

Direct visualization of a two-dimensional topological insulator in the single-layer $1T'$ -WTe₂

Zhen-Yu Jia,¹ Ye-Heng Song,¹ Xiang-Bing Li,¹ Kejing Ran,¹ Pengchao Lu,¹ Hui-Jun Zheng,¹ Xin-Yang Zhu,¹ Zhi-Qiang Shi,¹ Jian Sun,^{1,2} Jinsheng Wen,^{1,2} Dingyu Xing,^{1,2} and Shao-Chun Li^{1,2,*}

¹National Laboratory of Solid State Microstructures, School of Physics, Nanjing University, Nanjing, Jiangsu 210093, China

²Collaborative Innovation Center of Advanced Microstructures, Nanjing University, Nanjing 210093, China

(Received 11 February 2017; revised manuscript received 5 April 2017; published 7 July 2017)

We have grown nearly freestanding single-layer $1T'$ -WTe₂ on graphitized $6H$ -SiC(0001) by using molecular beam epitaxy (MBE), and characterized its electronic structure with scanning tunneling microscopy/spectroscopy (STM/STS). The existence of topological edge states at the periphery of single-layer WTe₂ islands was confirmed. Surprisingly, a bulk band gap at the Fermi level and insulating behaviors were also found in single-layer WTe₂ at low temperature, which are likely associated with an incommensurate charge order transition. The realization of two-dimensional topological insulators (2D TIs) in single-layer transition-metal dichalcogenide provides a promising platform for further exploration of the 2D TIs' physics and related applications.

DOI: [10.1103/PhysRevB.96.041108](https://doi.org/10.1103/PhysRevB.96.041108)

Two-dimensional topological insulators (2D TIs) feature conducting edge states topologically protected from backscattering by time reversal symmetry and a gapped bulk band structure, thus hosting the quantum spin Hall (QSH) effect [1–4]. This extraordinary property makes 2D TIs promising in future applications such as low dissipation electronics, quantum computing, etc. Since the discovery of the QSH effect in HgTe/CdTe quantum wells [5,6], many theoretical predictions have been made, aiming for more practical QSH materials [7–9]. However, it still remains difficult to realize the QSH effect in a natural single-layer 2D material in a well-controlled fashion [10,11]. Recently, Reis *et al.* has achieved bismuthene on a SiC substrate, and observed both conductance edge channels and a large band gap [12]. Although mechanical exfoliation has become the widely accepted method for achieving single-layer QSH materials [13,14], the samples have to be carefully safeguarded from contamination or reactions. Studies on 2D TI quantum wells have suffered from a lack of sophisticated growth techniques [6,15,16]. Characterizations of topological band structures have mostly focused on the surfaces of their bulk counterparts because of the limited availability of single-layer 2D TIs [10,17–20], in which the interlayer coupling has to be considered.

Recently, Qian *et al.* [9] predicted a family of large band gap QSH materials in the $1T'$ phase of transition-metal dichalcogenide (TMD), TX_2 , where T is a transition-metal atom (Mo, W), and X is a chalcogen atom (S, Se, or Te). These QSH materials are readily used to construct van der Waals (vdW) devices [9]. Additionally, the three-dimensional (3D) bulk forms of TX_2 , in particular, WTe₂ and MoTe₂, also exhibit exotic physics such as a type-II Weyl semimetal and unsaturated magnetoresistance [21,22]. Since TMDs boast outstanding properties such as chemically inert surface and weak interlayer interactions, the single-layer $1T'$ phase TMD is expected to display great potential once the topological edge states are experimentally confirmed. A recent transport study has shown convincing evidence for conducting edge channels in exfoliated $1T'$ -WTe₂ [13]. However, real-space imaging of

these edge states that reveals, e.g., its spatial width, its relation to the edge geometry, and its relation to other spectral features of the $1T'$ -WTe₂ surface is still lacking.

In this Rapid Communication, we have directly grown single-layer $1T'$ -WTe₂ on a graphitized $6H$ -SiC(0001) substrate by using molecular beam epitaxy (MBE), and we have *in situ* characterized the band structure with atomic-scale scanning tunneling microscopy/spectroscopy (STM/STS). Through these measures, any possible contamination from air or during transport was avoided, and an intrinsic electronic structure of monolayer WTe₂ was made available. The growth of monolayer WTe₂ was monitored by using reflection high-energy electron diffraction (RHEED). It has been found that the topological edge states are located along all kinds of WTe₂ step edges. The measured STS results are consistent with the calculated band structure based on the many-body effect [9]. However, in contrast to the semimetal behavior as predicted by density functional theory (DFT) [9], a bulk band gap is observed at the Fermi energy at low temperature, thus leading to the insulating behavior of single-layer WTe₂. Concomitantly, an incommensurate charge order is found to occur at low temperature, which is likely to be associated with a gap opening.

Single-layer WTe₂ films were grown in ultrahigh vacuum with a base pressure of 1×10^{-10} mbar. The $6H$ -SiC(0001) substrate was initially outgassed at $\sim 600^\circ\text{C}$, and then flashed up to $\sim 1350^\circ\text{C}$ for a few cycles until bilayer graphene (BLG) termination was achieved. The quality of the BLG/SiC(0001) was checked by RHEED and STM. High-purity W (99.999%) and Te (99.999%) were evaporated from an *e*-beam evaporator and a Knudsen cell. The temperature of the substrate was kept at $\sim 250^\circ\text{C}$ during WTe₂ growth, with a flux ratio of $\sim 1 : 20$ (W:Te). *In situ* STM/STS measurements were carried out with a low-temperature STM (Unisoku USM1600) at ~ 4.7 K, unless otherwise specified. STM measurements were performed with a constant current mode. A lock-in amplifier was used for the STS measurements, with an ac modulation of 5–10 mV at 963 Hz. Electrical resistance measurements were conducted in a physical property measurement system (PPMS) from Quantum Design. For *ex situ* resistance measurements, we deposited the Te capping layers on top of a single-layer WTe₂ film.

*scli@nju.edu.cn

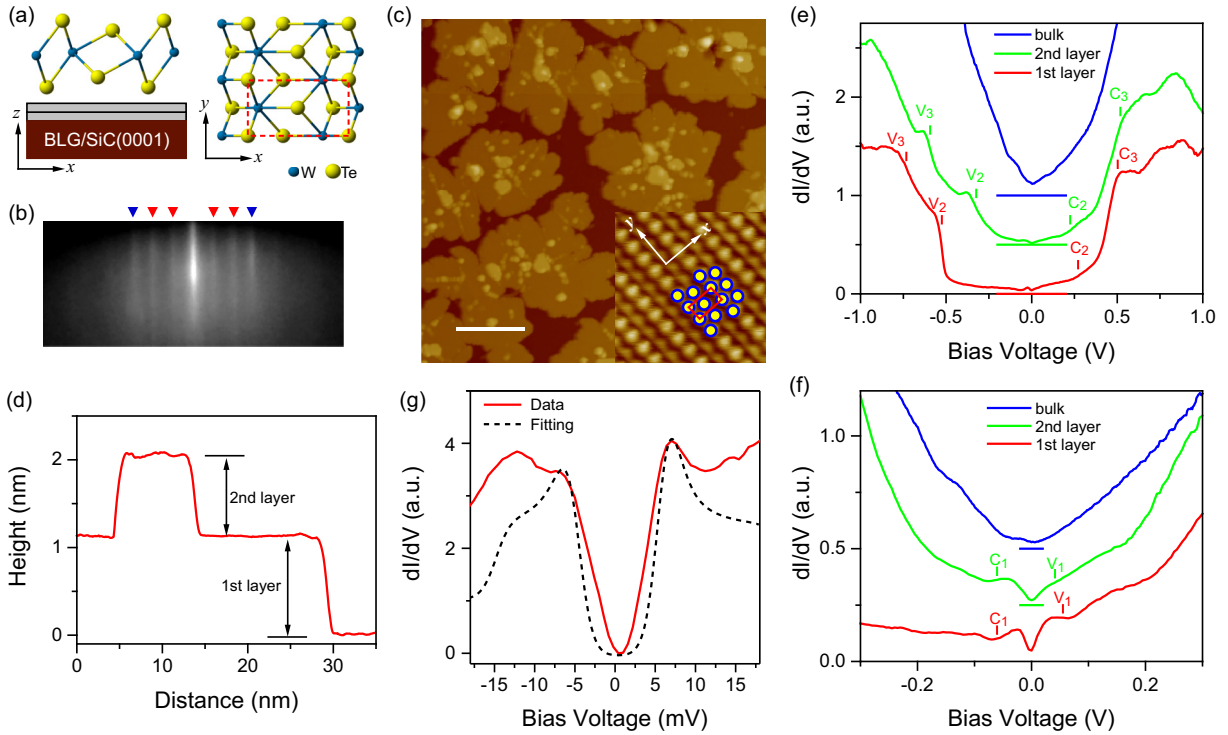


FIG. 1. Single-layer WTe_2 islands grown on BLG/SiC(0001). (a) Top and side view sketches of single-layer $1T'$ - WTe_2 on BLG/SiC(0001); (b) RHEED pattern of as-grown single-layer WTe_2 . The blue arrow marks the streaks from the BLG/SiC(0001) substrate, while the red arrows represent the ones from WTe_2 domains of three equivalent orientations. (c) Large-scale STM topographic image of single-layer WTe_2 islands on the BLG/SiC(0001) substrate ($150 \times 150 \text{ nm}^2$, $U = +1.0 \text{ V}$, $I_t = 100 \text{ pA}$, $T \cong 4.7 \text{ K}$). The length of the scale bar is 30 nm. Inset: Atomic resolution STM image of the single-layer WTe_2 surface ($U = +50 \text{ mV}$, $I_t = 500 \text{ pA}$, $T \cong 4.7 \text{ K}$) showing that single-layer WTe_2 is in the $1T'$ phase. The red rectangle represents the surface unit cell. (d) Line scan profile taken across both the first- and the second-layer WTe_2 . (e) dI/dV spectra taken on surfaces of single-layer WTe_2 (red), second-layer WTe_2 (green), and the bulk termination (blue), respectively. The labels C2, C3 and V2, V3 mark the edges of valence bands and conduction bands, according to the calculated band structure [9]. (f) Small energy scale (from -300 to $+300 \text{ mV}$) dI/dV spectra. (g) High-resolution dI/dV spectrum (red) taken at $\sim 6.7 \text{ K}$ indicating the features of the bulk band gap. Both the band gap and the coherence peaks are fitted (black dashed) based on a CDW gap format adopted from the literature [26].

Typically, the freestanding single-layer WTe_2 takes the $1T'$ crystal structure, as sketched in Fig. 1(a). The W atomic layer is sandwiched between the top and bottom Te atomic layers [23]. To achieve a quasifreestanding monolayer $1T'$ - WTe_2 , coupling to the substrate has to be efficiently reduced, which might otherwise destroy the topologically nontrivial edge states. Epitaxial bilayer graphene (BLG) formed on the $6H$ -SiC(0001) substrate was used, due to its chemically inert surface and vdW interlayer bonding [24]. WTe_2 prefers to grow in the layer-by-layer mode on BLG/SiC(0001) via optimizing the growth parameters (see the surface morphologies with various WTe_2 coverages in Fig. S1 in the Supplemental Material [25]). Figure 1(b) depicts the RHEED pattern of single-layer $\text{WTe}_2/\text{BLG}/\text{SiC}(0001)$. Pertaining to the symmetry registry between $1T'$ - WTe_2 (orthogonal) and graphene (hexagonal), there mainly exist three equivalent orientations of single-layer WTe_2 domains at the BLG surface. Randomly oriented WTe_2 islands are also occasionally observed, implying weak coupling between WTe_2 and BLG/SiC(0001).

Figure 1(c) shows a typical STM topographic image of WTe_2 grown on BLG/SiC(0001) at a coverage of ~ 0.7 monolayers (MLs). The surface is dominated by single-layer

WTe_2 islands, with the exception of some small second-layer WTe_2 islands. An atomic resolution STM image clearly shows the locations of surface Te atoms, as marked by the colored dots in the inset to Fig. 1(c). The step height of the first single-layer WTe_2 is $\sim 1.21 \text{ nm}$, much larger than the step height for the bulk of 0.701 nm [23], thus indicating a large vdW gap between the BLG substrate and the WTe_2 monolayer [see the line cut profile in Fig. 1(d)].

A typical differential conductance dI/dV curve measured on the terrace represents the bulk band structure of single-layer WTe_2 , as plotted at the bottom of Fig. 1(e). For comparison, the dI/dV curves measured on top of the second-layer and the bulk WTe_2 are also plotted together. The STS for single-layer WTe_2 is visually dissimilar from the bulk, because the single-layer energy band is well separated and two dimensional, while the bulk energy band is continuous and three dimensional. The band edges for the first single layer, as tentatively assigned according to the DFT calculations [9], agree greatly with the calculated band structure for freestanding single-layer WTe_2 with the many-body effect [see Fig. S1(F) in Ref. [9]]. Such a good agreement, particularly in this large energy range between $\pm 1 \text{ V}$ [9], further confirms the weak coupling of WTe_2

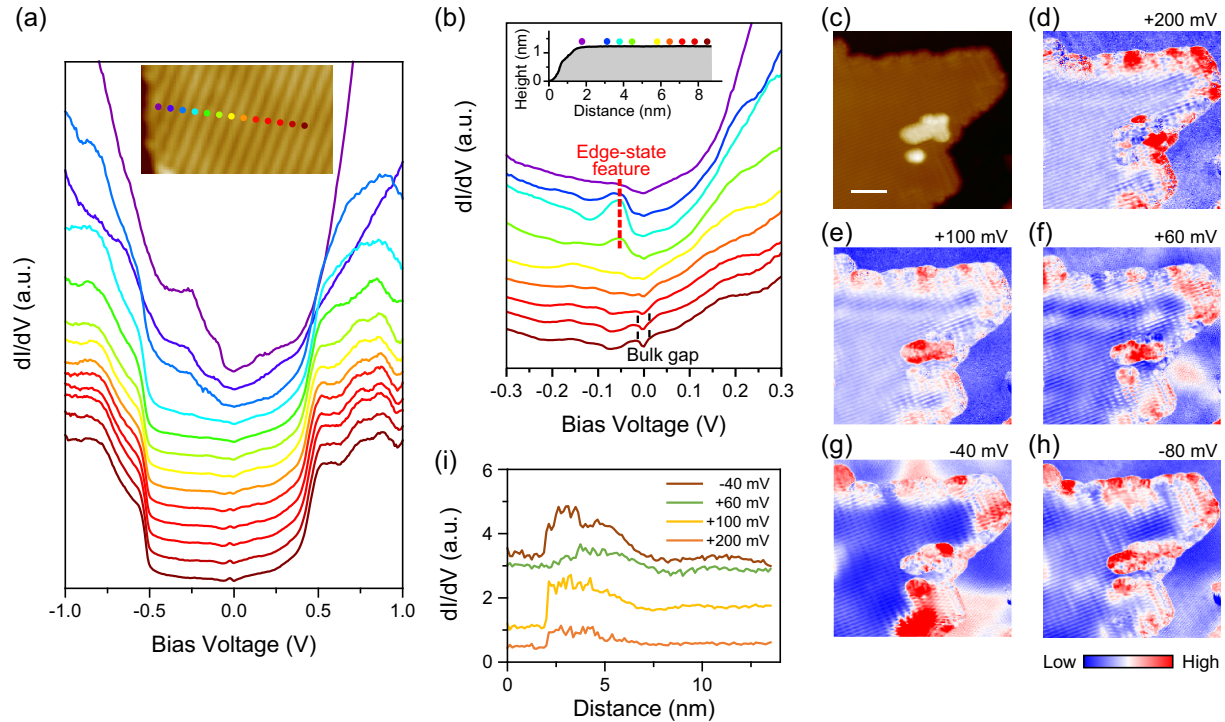


FIG. 2. Edge states of single-layer $1T'$ -WTe₂ on BLG/SiC(0001). (a) Large energy scale dI/dV spectra (from -1.0 to $+1.0$ V) taken along the rainbow-colored dotted line in the inset at ~ 4.7 K, sweeping from the terrace (red end) to the step edge (purple end). The inset shows the STM topographic image ($U = +500$ mV, $I_t = 200$ pA) where the dI/dV spectra were taken. The colored dots mark the locations where the same colored spectra were taken, respectively. (b) dI/dV spectra (from -300 to $+300$ mV) taken across the step edge. The corresponding line scan profile of the step edge is plotted in the inset, which is parallel to the y axis. The edge-state feature is marked by the red vertical line, and the bulk band gap by the black vertical lines. (c) STM topographic image ($28 \times 28 \text{ nm}^2$, $U = +1.0$ V, $I_t = 100$ pA). The length of the scale bar is 5.6 nm. (d)–(h) dI/dV maps measured on the same area of (c) with various bias voltages of $+200$, $+100$, $+60$, -40 , and -80 mV, respectively. (i) Typical line cuts extracted from (d)–(g) indicating the penetration length of the edge state is ~ 5.0 nm.

to BLG. The notable exception is that the density of states is drastically suppressed at the Fermi energy, indicating a gap is opened [see Fig. 1(f)]. In fact, the dI/dV intensity inside the gap is not suppressed to zero [see Fig. 1(f)], indicating it is not a full gap. The high-resolution dI/dV spectrum [Fig. 1(g)] shows coherence peaks at the gap edges. Such a gap is found ranging from ~ 20 to ~ 40 mV on the surface. The gap is most prominent in the first single layer, less in the second layer, and disappears in the bulk. The origin of the gap will be discussed below. It is worthwhile noting that the intensity between ~ -0.5 and $\sim +0.5$ eV is rather low for the first single-layer WTe₂, even though a nonzero density of states exists.

A spatially resolved differential conductance dI/dV spectrum represents the variation in the local density of states at the WTe₂ surface. The electronic structure near the periphery of the WTe₂ islands is disclosed in a series of dI/dV spectra taken along the line spanning from the step edge to the terrace, as shown in Fig. 2(a). The dI/dV intensity gradually increases as it approaches the step edge, especially in the bias range between ~ -0.5 and $\sim +0.5$ eV. The dI/dV spectra are also taken in a smaller bias energy range, from -300 to $+300$ mV [see Fig. 2(b)]. The feature located at ~ -40 mV is found to only exist near the step edge in a spatial range of ~ 5.0 nm, as marked by the red vertical line in Fig. 2(b).

Various orientations of the step edges are found in the periphery of the WTe₂ monolayer islands, which is different from a previous study for another 2D TI, ZrTe₅ [20]. In fact, the enhancement of the dI/dV intensities taking place along the step edges varies subtly, suggesting that the edge states are robust to the weak perturbations at the steps. Figures 2(c) and 2(d)–2(h) show a topographic image and the corresponding dI/dV maps taken at various bias energies, respectively. Evidently, the edge states, as indicated by the enhanced dI/dV intensity, are always distributed along the WTe₂ steps. The penetration length of the edge state is estimated to be ~ 5.0 nm, as shown in Fig. 2(i), in line with the predicted value given by Qian *et al.* [9]. Occasionally, the dI/dV intensities around the step edges exhibit an obvious discontinuity at certain bias energies, particularly in the upper left-hand corner of Figs. 2(f) and 2(g). Such a discontinuity in the dI/dV maps may be caused by the hybridization between the edge states with the bulk states out of the bulk band gap.

Next, we continue to discuss the origin of the bulk band gap in single-layer WTe₂. To investigate the transport behavior when such a band gap is opened, temperature-dependent resistance is measured over a full layer of single-layer WTe₂ and is plotted in Fig. 3(a) [see Figs. S1(e) and S1(f) in the Supplemental Material [25] for the corresponding surface morphologies]. The resistance exhibits a sudden increase,

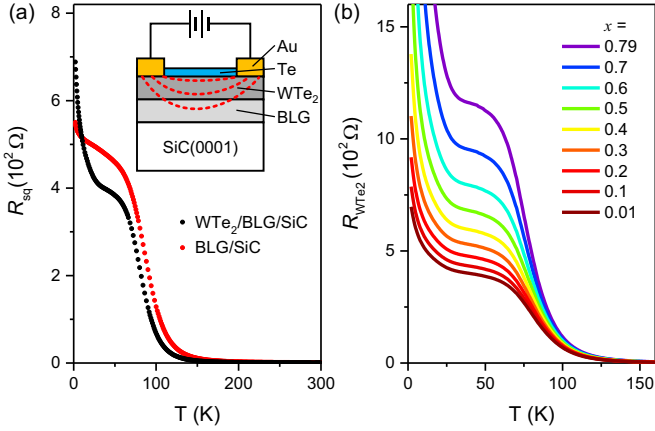


FIG. 3. Transport behavior of single-layer $1T'$ - WTe_2 . (a) The measured square resistance R_{sq} as a function of temperature. The black dotted line is R_{total} as measured on the Te-capped WTe_2 /BLG/SiC, and the red dotted line R_{BLG} as measured on the Te-capped BLG/SiC. The inset shows the schematic illustration of the resistance measurement. (b) The extracted effective resistance of single-layer WTe_2 , R_{WTe_2} , assuming $G_{total} = xG_{BLG} + G_{WTe_2}$, with various values of x . Here, $0 \leq x < x_m$ indicates the BLG/SiC substrate effect on G_{total} , with $x = 0$ standing for no substrate effect and $x = x_m$ corresponding to the maximal substrate effect.

followed by a kink as the temperature decreases to below ~ 100 K, and another insulating kink at ~ 30 K. For comparison, the resistance of the pure BLG/SiC(0001) substrate is also measured, as shown in Fig. 3(a). The entire behavior of WTe_2 /BLG/SiC(0001) from 300 K down to ~ 50 K might be easily attributed to the BLG/SiC(0001), while only the stronger insulating kink below ~ 30 K must be related to the $1T'$ - WTe_2 . To exclude a possible contribution from the BLG/SiC(0001) substrate, a two-channel model is assumed, as shown in the inset to Fig. 3(a). The measured conductance $G_{total} = G_{WTe_2} + xG_{BLG}$, and $0 \leq x < x_m$ presents the BLG/SiC substrate effect, with $x = 0$ standing for no substrate effect and $x = x_m$ the maximal substrate effect. It then follows that the effective resistance of WTe_2 , $R_{WTe_2} = R_{total}/(1 - xR_{total}/R_{BLG})$. Figure 3(b) shows the extracted R_{WTe_2} with various x values. Regardless of the values of the x factor, it is evident that the WTe_2 single layer behaves as an insulator at low temperature ($T \lesssim 30$ K).

Figure 4 shows typical STM topographic images and the corresponding fast Fourier transforms (FFTs) taken at negative biases at various temperatures. In addition to the Bragg peaks corresponding to the lattice unit along the x and y axes, as marked by the red circles, extra peaks are clearly identified at ~ 4.7 K, as marked by the blue circles. Such a FFT peak corresponds to a spatial charge periodicity of ~ 3.3 times of the unit size along the y axis. Such a charge order can persist up to LN_2 temperature, but disappears at room temperature, indicating that a charge order transition may occur between LN_2 and room temperature, as characterized in both STM images and the FFT. In general, quasiparticle interference (QPI) occurring at the step edge induces spatial charge modulations, but with a periodicity that is dependent on the bias energy. As seen in the topographic image and the corresponding FFT in Fig. 4, contributions from the

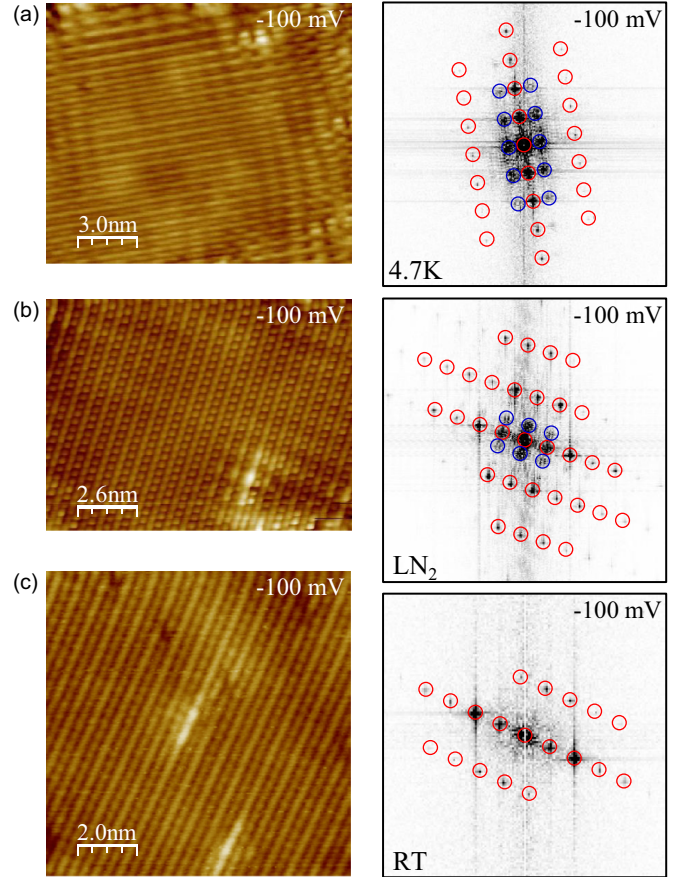


FIG. 4. Incommensurate charge order in single-layer $1T'$ - WTe_2 at low temperature. (a)–(c) STM topographic images (left panel) and the corresponding FFT (right panel) taken at ~ 4.7 K, LN_2 , and room temperature (RT), respectively. The bias voltages U are marked in the STM images, and $I_t = 0.1$ nA. The red circles in the FFT mark the Bragg vectors, and the blue ones the wave vector for incommensurate charge order.

tunneling electrons are integrated in the range from the Fermi level to the bias voltage, thus QPI-induced charge modulation appears to be smeared. Furthermore, the FFT transforms of the topographic images at different bias voltages indicate that the corresponding wave vector in reciprocal space does not change as the bias energy varies. Therefore, it is concluded that a static charge order exists.

All the experimental results point to the conclusion that single-layer $1T'$ - WTe_2 undergoes an incommensurate charge order transition and thus opens a band gap at the Fermi energy, turning the topological semimetal into a topological insulator at low temperature. The transition temperature for the incommensurate charge order obtained from STM data seems discrepant with that obtained from the transport result, which might be related to the multiple charge density wave (CDW) transitions as in TaS_2 or to Te capping. Furthermore, the band gap and the coherence peaks can be well fitted with a CDW model [26] [see Fig. 1(g)]. The coincidence in the periodicity of the incommensurate charge order with the electron pockets located at $\pm \Lambda$ [9] implies that the electron-phonon or electron-hole interactions may play a role in driving such a transition, which is expected to be greatly enhanced in the single-layer

limit of 2D materials [27]. Additional in-depth investigations are required to uncover the mechanism for the charge order transition. In addition, recent theoretical studies also predicted a band gap as well when considering the many-body effect [14] or the uniaxial strain [28].

In summary, we directly grow single-layer $1T'$ -WTe₂ and *in situ* visualize its topological edge states. Single-layer WTe₂ is weakly coupled to the BLG/SiC(0001) substrate, thus exhibiting a nearly freestanding electronic structure. The incommensurate charge order transition at low temperatures opens a bulk band gap at the Fermi energy, thus making single-layer WTe₂ a true 2D TI. In addition, the local density of states is extremely low for the bulk band structure in a larger energy scale, particularly between ~ -0.5 and $\sim +0.5$ eV, and thus it is expected that the fermions of the topological edge states dominate over the band fermions in such a large

energy scale, which may lead to a prominent QSH effect at low temperatures. The epitaxial monolayer WTe₂ grown by MBE provides a contamination-free material basis for the QSH study and also facilitates device construction by vdW epitaxy of 2D functional materials.

Note added. Recently, we became aware two other relevant papers [29,30].

This work was supported by the Ministry of Science and Technology of China (Grants No. 2014CB921103, No. 2013CB922103, No. 2016YFA0300404, and No. 2015CB921202), by the National Natural Science Foundation of China (Grants No. 11374140, No. 11374143, No. 11674157, No. 51372112, and No. 11574133), and by NSF Jiangsu Province (No. BK20150012).

Z.-Y.J. and Y.-H.S. contributed equally to this work.

-
- [1] B. A. Bernevig and S. C. Zhang, *Phys. Rev. Lett.* **96**, 106802 (2006).
- [2] C. L. Kane and E. J. Mele, *Phys. Rev. Lett.* **95**, 146802 (2005).
- [3] M. Z. Hasan and C. L. Kane, *Rev. Mod. Phys.* **82**, 3045 (2010).
- [4] X.-L. Qi and S.-C. Zhang, *Rev. Mod. Phys.* **83**, 1057 (2011).
- [5] B. A. Bernevig, T. L. Hughes, and S.-C. Zhang, *Science* **314**, 1757 (2006).
- [6] M. König, S. Wiedmann, C. Brüne, A. Roth, H. Buhmann, L. W. Molenkamp, X.-L. Qi, and S.-C. Zhang, *Science* **318**, 766 (2007).
- [7] Y. Xu, B. H. Yan, H. J. Zhang, J. Wang, G. Xu, P. Z. Tang, W. H. Duan, and S. C. Zhang, *Phys. Rev. Lett.* **111**, 136804 (2013).
- [8] C. C. Liu, W. Feng, and Y. Yao, *Phys. Rev. Lett.* **107**, 076802 (2011).
- [9] X. Qian, J. Liu, L. Fu, and J. Li, *Science* **346**, 1344 (2014).
- [10] F. F. Zhu, W. J. Chen, Y. Xu, C. L. Gao, D. D. Guan, C. H. Liu, D. Qian, S. C. Zhang, and J. F. Jia, *Nat. Mater.* **14**, 1020 (2015).
- [11] J. Zhou, F. Liu, J. Lin, X. Huang, J. Xia, B. Zhang, Q. Zeng, H. Wang, C. Zhu, L. Niu, X. Wang, W. Fu, P. Yu, T. R. Chang, C. H. Hsu, D. Wu, H. T. Jeng, Y. Huang, H. Lin, Z. Shen, C. Yang, L. Lu, K. Suenaga, W. Zhou, S. T. Pantelides, G. Liu, and Z. Liu, *Adv. Mater.* **29**, 1603471 (2017).
- [12] F. Reis, G. Li, L. Dudy, M. Bauernfeind, S. Glass, W. Hanke, R. Thomale, J. Schäfer, and R. Claessen, *arXiv:1608.00812*.
- [13] Z. Fei, T. Palomaki, S. Wu, W. Zhao, X. Cai, B. Sun, P. Nguyen, J. Finney, X. Xu, and D. H. Cobden, *arXiv:1610.07924*.
- [14] F. Zheng, C. Cai, S. Ge, X. Zhang, X. Liu, H. Lu, Y. Zhang, J. Qiu, T. Taniguchi, K. Watanabe, S. Jia, J. Qi, J. H. Chen, D. Sun, and J. Feng, *Adv. Mater.* **28**, 4845 (2016).
- [15] I. Knez, R.-R. Du, and G. Sullivan, *Phys. Rev. Lett.* **107**, 136603 (2011).
- [16] L. Du, I. Knez, G. Sullivan, and R. R. Du, *Phys. Rev. Lett.* **114**, 096802 (2015).
- [17] I. K. Drozdov, A. Alexandradinata, S. Jeon, S. Nadj-Perge, H. Ji, R. J. Cava, B. A. Bernevig, and A. Yazdani, *Nat. Phys.* **10**, 664 (2014).
- [18] S. H. Kim, K.-H. Jin, J. Park, J. S. Kim, S.-H. Jhi, T.-H. Kim, and H. W. Yeom, *Phys. Rev. B* **89**, 155436 (2014).
- [19] C. Pauly, B. Rasche, K. Koepf, M. Liebmann, M. Pratzner, M. Richter, J. Kellner, M. Eschbach, B. Kaufmann, L. Plucinski, C. M. Schneider, M. Ruck, J. van den Brink, and M. Morgenstern, *Nat. Phys.* **11**, 338 (2015).
- [20] X. B. Li, W. K. Huang, Y. Y. Lv, K. W. Zhang, C. L. Yang, B. B. Zhang, Y. B. Chen, S. H. Yao, J. Zhou, M. H. Lu, L. Sheng, S. C. Li, J. F. Jia, Q. K. Xue, Y. F. Chen, and D. Y. Xing, *Phys. Rev. Lett.* **116**, 176803 (2016).
- [21] M. N. Ali, J. Xiong, S. Flynn, J. Tao, Q. D. Gibson, L. M. Schoop, T. Liang, N. Haldolaarachchige, M. Hirschberger, N. P. Ong, and R. J. Cava, *Nature (London)* **514**, 205 (2014).
- [22] A. A. Soluyanov, D. Gresch, Z. Wang, Q. Wu, M. Troyer, X. Dai, and B. A. Bernevig, *Nature (London)* **527**, 495 (2015).
- [23] P. Lu, J.-S. Kim, J. Yang, H. Gao, J. Wu, D. Shao, B. Li, D. Zhou, J. Sun, D. Akinwande, D. Xing, and J.-F. Lin, *Phys. Rev. B* **94**, 224512 (2016).
- [24] C. Berger, Z. Song, X. Li, X. Wu, N. Brown, C. Naud, D. Mayou, T. Li, J. Hass, A. N. Marchenkov, E. H. Conrad, P. N. First, and W. A. de Heer, *Science* **312**, 1191 (2006).
- [25] See Supplemental Material at <http://link.aps.org/supplemental/10.1103/PhysRevB.96.041108> for STM topographic images for the WTe₂/BLG/SiC surface at various coverages.
- [26] U. Chatterjee, J. Zhao, M. Iavarone, R. Di Capua, J. P. Castellano, G. Karapetrov, C. D. Malliakas, M. G. Kanatzidis, H. Claus, J. P. Ruff, F. Weber, J. van Wezel, J. C. Campuzano, R. Osborn, M. Randeria, N. Trivedi, M. R. Norman, and S. Rosenkranz, *Nat. Commun.* **6**, 6313 (2015).
- [27] X. Xi, L. Zhao, Z. Wang, H. Berger, L. Forro, J. Shan, and K. F. Mak, *Nat. Nanotechnol.* **10**, 765 (2015).
- [28] H. Xiang, B. Xu, J. Liu, Y. Xia, H. Lu, J. Yin, and Z. Liu, *AIP Adv.* **6**, 095005 (2016).
- [29] S. Tang, C. Zhang, D. Wong, Z. Pedramrazi, H.-Z. Tsai, C. Jia, B. Moritz, M. Claassen, H. Ryu, S. Kahn, J. Jiang, H. Yan, M. Hashimoto, D. Lu, R. G. Moore, C. Hwang, C. Hwang, Z. Hussain, Y. Chen, M. M. Ugeda, Z. Liu, X. Xie, T. P. Devereaux, M. F. Crommie, S.-K. Mo, and Z.-X. Shen, *arXiv:1703.03151*.
- [30] L. Peng, Y. Yuan, G. Li, X. g Yang, J.-J. Xian, C.-J. Yi, Y.-G. Shi, and Y.-S. Fu, *arXiv:1703.05658*.